Journal of Power Sources 273 (2015) 638–644

Contents lists available at ScienceDirect

Journal of Power Sources

journal homepage: www.elsevier.com/locate/jpowsour

A stable silicon anode based on the uniform dispersion of quantum dots in a polymer matrix

Lanlan Zhong [a], Juchen Guo [a, b], Lorenzo Mangolini [a, c, *]

[a] Materials Science and Engineering Program, University of California, Riverside, United States
[b] Chemical and Environmental Engineering Department, University of California, Riverside, United States
[c] Mechanical Engineering Department, University of California, Riverside, United States

HIGHLIGHTS

- Silicon quantum dots have been uniformly dispersed in a polymer matrix.
- Annealing leads to the formation of an amorphous carbon matrix.
- The hybrid structure is stable under cycling for 200 cycles.
- The coulombic efficiency exceeds 99.8%.

ARTICLE INFO

Article history:
Received 27 July 2014
Received in revised form
23 September 2014
Accepted 24 September 2014
Available online 2 October 2014

Keywords:
Silicon
Lithium ion
Anode
Polymer

ABSTRACT

We propose a novel approach to the fabrication of silicon-containing anodes for lithium-ion batteries. Our approach is based on a liquid dispersion comprising of silicon quantum dots, carbon nanotubes and polyvinylpirrolidone (PVP) as a polymer additive. Coating of this dispersion onto copper foil followed by annealing in inert atmosphere allows the realization of a structure with good electrical conductivity, high specific surface area and with a carbon-based coating preventing the direct contact between the silicon particles and the electrolyte. This structure maintains a specific charge capacity of approximately 1000 mAh g^{-1} for 200 cycles and reaches a coulombic efficiency of 99.8%. The addition of PVP is a simple and scalable way of realizing, after annealing, a carbon-based matrix which surrounds the silicon particles and which greatly enhances the stability of the battery. The proposed process is based on commercially available carbon nanotubes, on silicon quantum dots which are produced using a scalable plasma-enhanced chemical vapour deposition technique, and is compatible with large area coating and processing techniques. The fabrication protocol described in this contribution represents a step towards the successful commercial utilization of silicon-based nanomaterials for energy storage applications.

1. Introduction

Lithium ion batteries are the most widely used energy storage technology in portable electronics. Continuous improvements in their performance are highly desired especially to enable their use in automotive applications. Silicon is a promising alternative anode material with a capacity of 3579 mAh g^{-1} which is about a magnitude higher than that of graphite anode [1]. For this reason, silicon as anode material has been extensively studied in the last few years. Several factors still prevent its utilization in commercial batteries. Silicon has poor electrical transport properties compared to graphite, thus it needs to be used in combination with electrical conductive additives. It experiences large volume variations during battery charge/discharge resulting in pulverization of the active layer [2], leading to poor cycling stability and rapid capacity fading. The chemical stability of silicon with typical electrolyte formulations is poorly understood, and in particular the formation of a solid electrolyte interface (SEI) with poor mechanical stability [3] and with poor lithium ion transport properties [4–6] is believed to negatively affect the cyclability of silicon-containing structures. The loss of electrical contact between active materials and the current collector [4,7,8] is also a crucial problem, considering that the contact must be capable of accommodating for the large volume change of silicon.

* Corresponding author. Materials Science and Engineering Program, University of California, Riverside, United States.
E-mail address: lmangolini@engr.ucr.edu (L. Mangolini).

http://dx.doi.org/10.1016/j.jpowsour.2014.09.155
0378-7753/

The issue of the pulverization of the active material upon cycling can be resolved by using nanostructured silicon, such as nanowires [9–12], nanotubes [13] and nanoparticles [14,15]. For the case of nanoparticles, keeping the size below 150 nm has been found to prevent particle fracturing during lithiation/delithiation [15]. In order to maintain a good electrical conductivity, the addition of conductive additives is necessary. Graphite [16–20], graphene [21–25], carbon nanotubes [3,7,26–28] have been used for this purpose. Finally, several reports suggest that over-coating the silicon surface with a carbon-based layer is a promising strategy to enhance the stability of the anode [12,13,29]. The exact mechanism of stabilization imparted by the carbon coating is under continuous investigation.

To summarize, a critical analysis of the vast literature on this topic suggests that a viable silicon-based anode requires the use of small silicon nanostructures which are firmly in contact with a current-carrying element (typically a carbon-based structure) and which are protected with a carbon-based coating. Moreover, the scalability of the fabrication method with which this structure is realized is important, given the large-scale requirements of the energy-storage market. With this study we propose a fabrication approach that is scalable, compatible with large-scale manufacturing requirements and that achieves a structure that satisfies the conditions summarized above. Our fabrication protocol is based on the non-thermal plasma synthesis of silicon nanoparticles [30,31], a technique which has emerged as a promising candidate for the high-rate production of high-quality, freestanding silicon nanoparticles. This technique is capable of producing up to hundreds of milligram per hour of silicon particles smaller than 10 nm, with a narrow size distribution (all particles are below 10 nm in size) and with precursor utilization that approaches unity when silane (SiH_4) is used as precursor, and that exceeds 50% when silicon tetrachloride is used as precursor [31]. We functionalize the silicon particle surface and combine it with commercially available carbon nanotubes and a common polymer (polyvinylpyrrolidone, or PVP) to form a liquid dispersion that can then be applied using standard coating techniques to the desired surface, such as copper foil. The liquid dispersion approach is compatible with large-volume coating techniques such as roll-to-roll slot die coating. Annealing at a temperature of 500–550 °C leads to the decomposition of the polymer additive and to the formation of a carbonaceous structure which is responsible for a significant improvement in battery stability compared to the structure without any PVP additive.

The paper is organized as following: the synthesis and processing protocol is first discussed, followed by a description of the techniques used for materials characterization and for the measurement of the electrochemical half-cell performance. The results for our proposed structure and for carefully designed control experiments are then presented and discussed.

2. Experiment

2.1. SiQDs synthesis and surface chemical modification

Crystalline silicon nanoparticles with a narrow size distribution were produced using the non-thermal plasma technique described in Ref. [30]. The process is easily scalable and converts the precursor (silane) into nanoparticles with a utilization rate that can approach unity with an optimized reactor design [31]. For this study, silicon quantum dots (SiQDs) were prepared in a 1/2″ outer diameter Pyrex reactor with a flow rate of 150 sccm of 1.37% SiH_4 in argon. The reactor pressure was 3.0 Torr. 100 sccm of H_2 were added at the exit of the plasma volume via a side gas inlet to increase the surface coverage with hydrogen [32]. This additional exposure to hydrogen enhances the reactivity of the surface with ligands such as alkenes [32]. The electrical power supplied by the radio frequency (RF) generator was 35 Watts, sufficient to create particles with a crystalline structure. The <10 nm silicon nanoparticles are collected at the exhaust of the plasma reactor via filtering and transferred into a glove box while carefully avoiding oxygen exposure. Surface modification with 12-carbon long chains is performed with the goal of preventing oxidation and of stabilizing the SiQDs in organic solvents such as chloroform or toluene. Organic aliphatic chains are grafted on the surface of silicon nanoparticles by refluxing the nanoparticles in a 1-dodocene/mesitylene (1:4 v%) mixture. Before reaction, high purity argon was bubbled through all solvents and reactants to minimize the oxygen level, and molecular sieve were used to remove water traces. The alkylation reaction typically lasts for 4 h at the solvent boiling point (164.7 °C). After surface modification the particles are separated by evaporating the solvent with mild heat under vacuum. Fourier transform infrared spectroscopy (FTIR) measurements, shown in Fig. S1 of the supplementary information file, confirm that the surface modification reaction is successful [33,34].

2.2. Si-QDs-PVP-CNTs composites fabrication

Multiwall carbon nanotubes (part number 724,769 from Sigma Aldrich, OD × L 6–9 nm × 5 um) and polyvinylpyrrolidone (PVP), (part number PVP-40 from Sigma Aldrich, 40,000 molecular weight) were used as received. In a typical preparation procedure, 10 mg of functionalized SiQDs and 10 mg of PVP are disperse in chloroform and bath sonicated for 5 min 2.5 mg of CNTs are then added to this solution and the mixture is probe sonicated for 5 min. The weight distribution of the composing elements in the dispersion is thus 4:1:4 of SiQDs:CNT:PVP. The SiQDs are the active element of the formulation and the CNTs provide efficient electrical conductivity after coating and annealing of the dispersion. PVP is used as a precursor for the formation of an amorphous carbon matrix that acts as binder. No other binder is added to the liquid dispersion. A more detailed discussion of the effective weight distribution of the composing elements after thermal annealing is presented in the next section.

The same procedure is followed for the preparation of control samples without additives such as PVP. The dispersion is then applied to copper foil by drop-casting. The coating is then dried and baked in a tube furnace under a continuous flow of argon (25 sccm) at a pressure of 0.21 Torr. The leakage rate of the annealing apparatus is below 0.03 Torr min^{-1}. The temperature is ramped up from 50 °C to 550 °C with increments of 100 °C, holding the temperature for 10 min at each step. After annealing, the weight loading is typically around 0.2 mg cm^{-2}.

2.3. Electrode preparation and electrochemical testing

After annealing, the copper foil with silicon-based coating is assembled into a coin cell battery which uses lithium foil as counter electrode. We use commercially available separator from MTI (Li-ion Battery Separator Film, Part number: EQ-bsf-0025-60C). 1 M $LiPF_6$ in ethylene carbonate/diethyl carbonate (1:1 v/v) was used as the electrolyte (from MTI, Electrolyte $LiPF_6$, part number: EQ-Be-LiPF6). All cells are cycled between 0 V and 1.5 V. The charge capacity is measured at a using a potentiostat from Arbin Instruments. Cyclic voltammetry (CV) is performed at a sweeping rate of 0.1 mV s^{-1} using modelVMP3 from BioLogic Science.

2.4. Materials characterization

We use a variety of techniques to characterize the material under investigation. Scanning electron microscopy (SEM) is

performed on a Nova NanoSEM 450. Transmission electron microscopy is performed by scratching some of the active layer onto a lacey carbon TEM grid (from Ted Pella, product number: 01895-F) and by analysing it using a Tecnai T12 120 kV instrument. Raman is performed using a Horiba LabRam system with a 532 nm laser source. X-ray diffraction (XRD) is performed on a PANalytical EMPYREAN instrument with a CuKα source. Thermal gravimetric analysis is conducted by using a Seiko 220U TG-DTA instrument. Fourier Transform Infrared (FTIR) spectroscopy is done using a modular spectrometer from Newport-Oriel. Samples for FTIR are prepared either by drop-casting a dispersion onto a reflective surface and by performing diffuse reflective (DRIFT) measurements, or by using a zinc selenide ATR crystal.

3. Results and discussion

Fig. 1a shows a top-down SEM micrograph of a coating obtained by drop-casting a SiQDs-PVP-CNT dispersion onto copper foil. The carbon nanotubes appear to be uniformly coated with a nanostructured layer. Fig. 1b has been obtained by drop-casting the same dispersion onto a TEM grid. The carbon nanotube backbone is coated with a layer whose thickness (around 10 nm) is consistent with the size of the silicon particles. For comparison we also show in Fig. 1c a top-down SEM micrograph of a coating obtained using a dispersion of carbon nanotubes alone. The clear difference with respect of Fig. 1a further supports the conclusion that a uniform coating of silicon particles is obtained around the carbon nanotubes. Without any additional processing this structure has poor electrochemical performance, most likely because of the poor electrical contact between the particles and the nanotubes. This is due to the presence of relatively long aliphatic chains grafted to the particle surface, and by the presence of the polymer additive. The device functionality is enabled by annealing at moderately high temperatures in an inert atmosphere. We have tested different annealing temperatures and have found that the best performance with respect of both capacity and stability is obtained at 500 °C. The discharge capacity and the Coulombic efficiency of the anodes as a function of annealing temperature are shown in Fig. S2 of the supplementary information file. During thermal annealing we observe significant restructuring of the anode. In Fig. 1d we show the top-down SEM micrograph of the coating shown in Fig. 1a after thermal annealing at 550 °C. The silicon particles tend to agglomerate into clumps with a size of few tens to hundreds of nanometres. At this point we have been unable to avoid this restructuring, which is probably due to the decomposition of the polymer additive during the annealing process. We have performed TEM on the resulting structure by scratching some material off the surface of the annealed coating and by then applying it onto a lacey carbon TEM grid. The individual quantum dots are still clearly distinguishable in the large agglomerates, as shown in Fig. 1e. A combination of dark field imaging and selected area diffraction (Fig. 1f and its inset, respectively) leads to the conclusion that the agglomerates are comprised of silicon nanocrystals. The particles do not coalesce into large crystals or denser agglomerates. A series of higher magnification TEM images, shown in the supplemental material (Figs. S3 to S11), confirms the presence of nanocrystals within the large agglomerates. Analysis of the higher magnification images confirms that the lattice fringes have a spacing corresponding to that of [111] silicon planes. These higher magnification images also suggest that the silicon quantum dots are surrounded by a uniform layer of amorphous material, whose properties are going to be discussed in details later in this contribution.

Despite the spatial rearrangement of the silicon particles during annealing, this structure achieves a very promising electrochemical performance. In Fig. 2 we show the discharge capacity plotted against the number of charge–discharge cycles. The first discharge

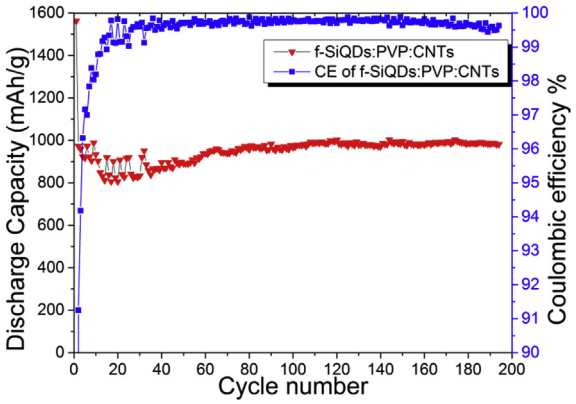

Fig. 2. Discharge capacity (mAh g^{-1}) and coulombic efficiency over number of charge–discharge cycles for the sample shown in Fig. 1(d).

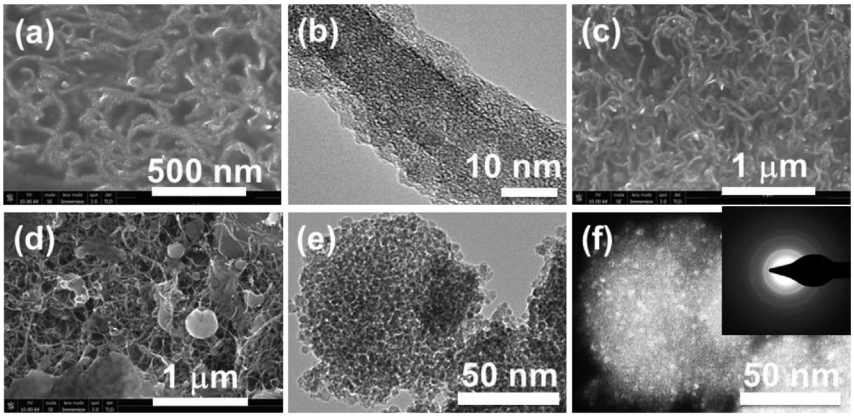

Fig. 1. (a) SEM of a coating generated by drop-casting a dispersion of silicon quantum dots, carbon nanotubes and PVP onto a copper film. (b) TEM of silicon quantum dots and PVP coating a multi-walled carbon nanotube. (c) Same as (a) but without the silicon quantum dots. (d) Same as (a) but after annealing at 550 °C in argon. Restructuring of the coating takes place during the annealing process. In particular, the silicon particles agglomerate into larger clumps. (e) TEM of a clump of silicon particles resulting from the annealing process. The sample is prepared by gently scratching the sample shown in (d), by dispersing the material in methanol and by drop-casting onto the TEM grid. (f) Dark field of (e) confirming the presence of nanocrystals. In the inset of (f) the selected area diffraction pattern for the particles shown in (e) and (f) is shown. An area including a large number of particles is selected to generate the pattern.

cycle achieve a capacity of 1600 mAh g^{-1}, which quickly decays to 1000 mAh g^{-1}. This value is then maintained for 200 cycles. The Coulombic efficiency, while being low for the first few cycles, reaches a stable value of 99.8% before starting to decrease close to the 200th cycle. In Fig. 3 we show the results of the cyclic voltammetry measurements from the first to the third cycle. Broad delithiation and lithiation peaks at 0.53 V and 0.18 V respectively are observed, consistent with previous studies on silicon-based anodes. During the first cycle a peak due to the SEI layer formation at 0.74 V is observed [5,23,35,36]. The 0.18 V lithiation peak become more distinguishable in the 2nd and 3rd cycles, a behaviour which has been reported in several other contributions [22,37–39] and that has been attributed to the structural change of the silicon particles after the first charge–discharge cycles (from crystalline to amorphous) [40]. The half-cell capacity measurement has been performed at a charge and discharge rate of 0.1 C, calculated based on the sum weight of the silicon quantum dots and carbon nanotubes coated onto the copper substrate. This approximation would be correct under the assumption that the polymer is completely removed from the coating during the annealing process. Our temperature-controlled gravimetric analysis (TGA) measurements show that PVP is not completely removed during the annealing process, although the error introduced into the calculation of the specific charge capacity is small.

The TGA scan for our SiQDs:CNT:PVP sample, together with the corresponding differential (DTGA) analysis, is shown in Fig. 4. We have normalized the data so that the weight fraction is 100% at 100 °C, i.e. after an initial weight loss due to the removal of residual solvent from the film. Weight loss occurs around 150 °C and at 350 °C. Both these peaks are consistent with TGA data reported in the literature for PVP [41,42]. Based on the initial weight distribution in the dispersion of 4:1:4 of SiQDs:CNT:PVP, we find that the decomposition of PVP at high temperature leads to the presence of a residue in the annealed structure. This is to be expected for the case of PVP, which is known to decompose into a carbonaceous structure with a mass yield between 4% and 15% depending on the annealing conditions and on the presence of other additives mixed with the PVP [41]. Based on the TGA measurement we estimate a final composition of 4:1:0.4 of SiQDs:CNT:(PVP decomposition product), corresponding to ~10% mass yield from the PVP decomposition. This does not account for the weight change due to reaction between the PVP and the silicon particles during the annealing reaction, which may lead to the formation of silicon carbide (as it will be more extensively discussed). If we correct the specific charge capacity data to account for the carbon residue from the PVP decomposition, we find that the battery maintains a reversible capacity of 925 mAh g^{-1} for up to 200 cycles. Under the assumption that the charge storage is performed by silicon only (consistently with the voltammetry data), we calculate that silicon achieves a reversible charge capacity of 1250 mAh g^{-1} for up to 200 cycles.

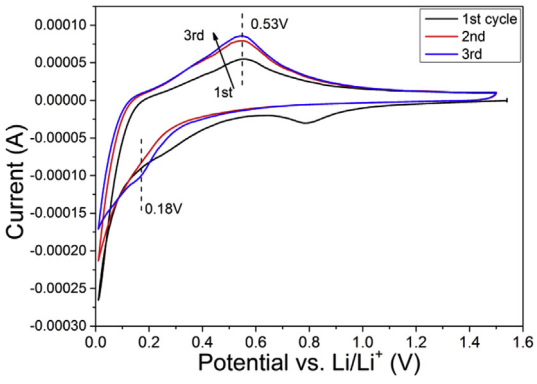

Fig. 3. Cyclic voltammetry of the sample shown in Fig. 1(d).

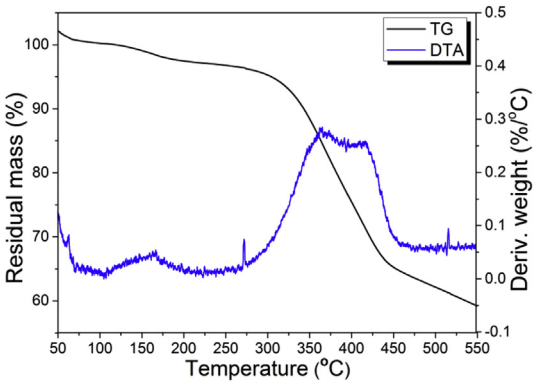

Fig. 4. TGA of the coating prepared from the 4:1:4 liquid dispersion of SiQDs:CNT:PVP. The negative of the differential of the TGA scan is also shown to highlight the decomposition temperature.

We point out that we selected PVP as an additive because of the good compatibility between PVP and carbon nanotubes [43,44] and because of PVP is soluble in chloroform, which is compatible with the functionalized silicon quantum dots. Fig. 1a confirms the compatibility of these components. We have found that PVP is not only necessary at obtaining a conformal coating of silicon nanoparticles onto the carbon nanotubes, but it also acts a precursor for the formation of a carbonaceous layer that entraps the silicon particles. A detailed discussion of the nature of this carbonaceous layer is now presented.

We have first performed x-ray diffraction (XRD) on the annealed coating and on a control sample in which only silicon nanoparticles are present in the coated layer. After thermal annealing, XRD analysis of the full SiQDs:CNT:PVP coating (see Fig. 5, top spectrum) shows peaks due to the carbon nanotubes (26.5° for the [002] plane and 44.6° for the [101] plane) and to the silicon nanocrystals ([111] at 28.4°, [220] at 47.3°, [311] at 56.1°, [400] at 69.1°, [331] at 76.4°, [422] at 88.1° and [511] at 95°). The [111] and [200] peaks from the copper substrate at 43.3° and 50.5° respectively are also clearly distinguishable. The peak assignment is based on the ICSD database (Inorganic crystal structure database FIZ Karlsruhe). We could not resolve any contribution from crystalline silicon carbide. Analysis of the grain size using Scherrer's formula returns a value of 3.9 nm for the silicon particle size after annealing. The control experiment, i.e.

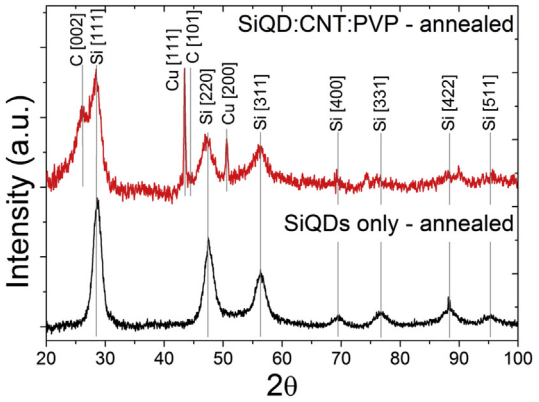

Fig. 5. X-ray diffraction for the sample obtained by annealing the dispersion of SiQDs:CNT:PVP. Clear peaks from crystalline silicon, from graphite and from the copper substrate are distinguishable (top spectrum). As a reference we also show the x-ray diffraction spectrum for silicon nanoparticles only (bottom spectrum), annealed using the same procedure.

the case of silicon nanoparticles only, is shown in Fig. 5, bottom spectrum. For this case the particles are annealed on a quartz slide using the same annealing cycle followed for the sample shown in the top spectrum of Fig. 5, but without any carbon nanotubes, without any PVP and without functionalizing the particle surface. The particle size in this case, calculated using Scherrer's formula, is 5.4 nm. This suggests that the presence of PVP and of the 12-carbon long chains at the particle surface is effective at preventing grain growth. Regarding silicon carbide, the absence of peaks in the XRD spectrum does not rule out that the reaction between silicon and the combination of 12-carbon long chains grafted at the particle surface and of the PVP leads to the formation of silicon carbide with an amorphous structure.

Extensive Raman characterization, shown in Fig. 6, supports the conclusion that the presence of a carbon precursor in the coating leads to the formation of both an amorphous carbon phase and of amorphous silicon carbide in the final structure. In Fig. 6a we show the Raman spectra for the silicon quantum dots functionalized with 1-dodecene. The particles were drop-cast onto a quartz slide, and due to the low thermal conductivity of the nanoparticle coating it is necessary to acquire this data using very low laser power, reducing the signal-to-noise ratio. Laser-induced heating introduces a shift in the crystalline silicon peak position to lower wavenumbers. We have made sure that no heating-induced shift is present for this sample, and we find the expected silicon peak at a position of 515 cm^{-1}. The shift compared to the bulk value of 521 cm^{-1} and the appearance of a shoulder at lower wavenumbers are well-known to be induced by the small size of the crystal [45–48]. For the case of

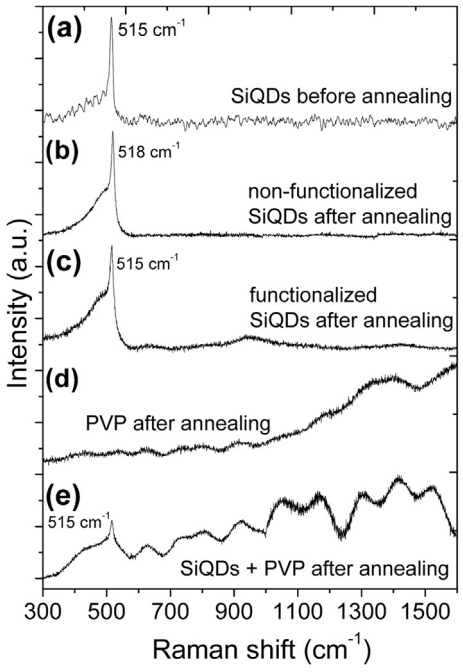

Fig. 6. Raman analysis of the materials under study. (a) Raman of functionalized silicon quantum dots before annealing. (b) Raman for silicon quantum dots after annealing. (c) Raman of 1-dodecene functionalized silicon quantum dots after annealing. The main feature related to the silicon nanocrystals is visible in (a), (b) and (c). A small broad peak around 900 cm^{-1} is distinguishable in (c) and attributable to amorphous silicon carbide (see text for complete discussion). (d) Raman of the product of decomposition of PVP, annealed using the same procedure used for the anode structure. Clear signature of graphitic carbon is present. (e) Raman of functionalized silicon quantum dots and PVP, after annealing. Features due to crystalline silicon, graphitic and amorphous carbon, and amorphous silicon carbide are distinguishable (please see text for complete discussion). Carbon nanotubes are not added to this sample to simplify the data interpretation.

non-functionalized silicon particles annealed using the same profile as for the anode (Fig. 6b) we also obtain only one feature corresponding to nanostructured silicon. The shift in the peak position to 518 cm^{-1} is consistent with a growth in crystallite size. Fig. 6c shows the Raman spectrum for silicon quantum dots functionalized with 1-dodecene and annealed at 550 °C. The main feature in this scan is the one from crystalline silicon. The peak position is 515 cm^{-1}, same as for the particles before annealing and lower than for the case of non-functionalized annealed particles (Fig. 6b). This suggests that the presence of the surface alkyl chains has prevented grain growth. Another small feature around 900 cm^{-1} is distinguishable and attributable to amorphous silicon carbide, as it will be discussed more extensively later in the manuscript. In Fig. 6d we show the Raman spectrum for the decomposition product of PVP, under the same annealing conditions. The broad features at 1350 cm^{-1} and 1580 cm^{-1} correspond to the D and G peaks from sp^2 carbon respectively [49–51]. Finally in Fig. 6e we show the spectrum for a mixture of functionalized silicon quantum dots and PVP, after annealing at 550 °C. The carbon nanotubes are not added to this mixture, since their expected contribution to the signal between 1300 cm^{-1} and 1600 cm^{-1} would make the interpretation of the spectrum more difficult. The peak corresponding to crystalline silicon is still present although its peak position is at 515 cm^{-1}. This is consistent with the previous XRD observation that the presence of the carbon precursor prevents grain growth during annealing. A significant shoulder is also present at lower wavenumber between 400 cm^{-1} and 450 cm^{-1}, consistent with the contribution which has been observed at low wavenumbers in various amorphous carbon structures [52–54]. The shape of the Raman spectrum in the 1100 cm^{-1} to 1600 cm^{-1} range is also significantly different than that of the spectrum shown in Fig. 6d. Raman analysis of carbon-based structures is known to be very sensitive to the degree of ordering in the film and to the ratio of sp^2 to sp^3 bonding [49–51]. The shift of the G band to lower wavenumber compared to the case shown in Fig. 6d can be attributed to a decrease in the fraction of graphite-like carbon in the film and to an increase in the presence of amorphous, sp^3 bonded carbon [49–51]. The additional peaks at 1150 cm^{-1} and 1450 cm^{-1} present in Fig. 6e compared to Fig. 6d have been assigned to trans-polyacetylene chains [55]. Overall, these data suggests that the presence of silicon nanoparticles dispersed within the PVP matrix leads to the formation of a carbon-based structure which is significantly different than what is obtained without silicon particles, following an identical annealing procedure. The authors in Ref. [51] also point out that a shift of the G peak to lower wavenumbers is observed for increasing silicon fraction for the case of amorphous silicon carbide alloys. This is consistent with an increase in the broad Raman scattering signal in the 600 cm^{-1} to 900 cm^{-1} range, which has been observed in amorphous silicon carbide films grown by plasma-enhanced chemical vapour deposition [56,57], in superlattices of silicon particles precipitated in an amorphous silicon carbide matrix [58,59], and has also been predicted by several theoretical studies (see for instance [60]). The data set strongly suggests that amorphous silicon carbide is formed during the annealing of the silicon nanoparticles in presence of PVP. It also indicates that the presence of the surface alkyl chains alone is not conducive to the formation of the carbon matrix (see Fig. 6c). The polymer not only helps dispersing the carbon nanotube in the desired solvent, but also acts as precursor for the formation of a carbon-based matrix. Finally in Fig. 7 we show the influence of the functionalization of the silicon nanoparticles and of the addition of PVP to the dispersion on the half-cell stability. We compare the performance of the anode based on the SiQD:CNT:PVP dispersion (same as the data shown in Fig. 2) with that of two structures, one based on a dispersion of alkylated silicon quantum dots and CNTs

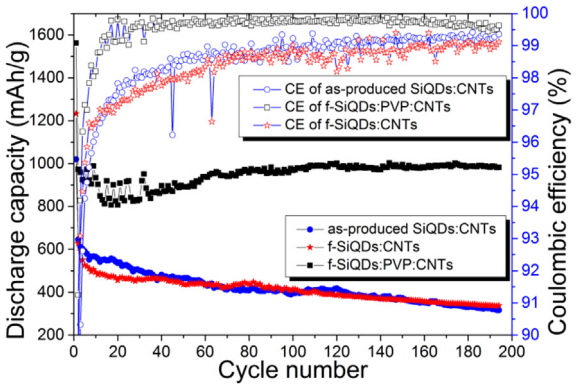

Fig. 7. Comparison of battery performance for the full anode (functionalized silicon quantum dots + PVP + CNT) with two control structures. The first control samples is realized using non-functionalized silicon particles and CNT, the second using functionalized silicon particles and CNT. For both the control structures PVP is not added to the liquid dispersion formulation.

and one based on a dispersion of non-functionalizes silicon quantum dots and CNTs. The same annealing procedure is used for these control anodes, and the main difference is that PVP is not added to the dispersion. Both control anodes achieve a significantly smaller capacity than the anode based on the full dispersion and also show a faster degradation in their performance. By the 200th cycle, the control anodes capacity has decayed to 400 mAh g^{-1}.

Based on the data shown here, we reach the following conclusions:

- The addition of the PVP to the dispersion formulation is critical for stabilizing the anode performance.
- The functionalization of the nanoparticle surface with alkyl chains is not sufficient at generating a carbon-matrix after annealing and does not lead to a half-cell with improved lifetime. We have found that the surface functionalization is effective at preventing sedimentation of the silicon particles in solution, thus improving the processability of our dispersion formulation.
- Annealing of the PVP-containing coatings leads to the formation of a carbon-based phase. This conclusion is supported by TGA and Raman data. Raman also suggests that amorphous silicon carbide is formed during the annealing step. This is due to the inevitable reaction between the silicon particles and the polymer during the high-temperature annealing. Nevertheless, the presence of this carbon-based phase in the final structure seems to provide a clear improvement with respect of cycling stability (see Fig. 7).
- The formation of silicon carbide may explain the relatively low first cycle capacity of the structure (~1600 mAh g^{-1}). Silicon carbide is inactive during the lithiation process [61,62]. The data discussed here suggest that some of the silicon is converted into silicon carbide during the annealing procedure, making a fraction of the silicon material effectively inactive. This problem is exacerbated by the small size of the particles. We are currently investigated the role of particle size on capacity and stability of the anode, and a future contribution will summarize our findings.

Our findings are consistent with those of several other groups that report that protecting the silicon surface with a carbon-based layer is effective at improving the anode lifetime [12,13,29]. The authors in Ref. [12] suggest that a carbon layer enhances the mechanical stability of the SEI while preventing the full lithiation of the silicon structure, thus limiting its capacity. The relatively small capacity of our structure may be partially explained by this argument, although (as already mentioned) a significant fraction of the particle volume may be converted into amorphous silicon carbide during annealing, further reducing charge capacity.

Our major finding is that the addition of an off-the-shelf polymer additive (PVP) to the silicon nanoparticle and carbon nanotube dispersion is effective at improving the half-cell stability. The combination of TGA, Raman and TEM analysis presented here confirms that the PVP acts as a precursor for the formation of a carbon-containing phase which is beneficial to the battery performance. This represents a simple strategy that could be implemented in large-scale manufacturing protocols.

To summarize, we have developed a dispersion based on functionalized silicon quantum dots, PVP and carbon nanotubes. Coating followed by the appropriate annealing cycle leads to the formation of a well-dispersed heterojunction of silicon particles and carbon nanotubes. When utilized as an anode for lithium ion batteries, this structure maintains a capacity of approximately 1000 mAh g^{-1} for 200 cycles. The silicon particles utilized in this study are produced using a scalable plasma-based synthesis technique which effectively converts silane into particles and that is expected to be scalable to large production rates. Moreover, the developed ink is expected to be compatible with large area, roll-to-roll coating techniques. The addition of PVP to the formulation, originally motivated by the need of improving the carbon nanotube dispersibility in the non-polar solvent of choice, has been found to be highly beneficial at enhancing the battery lifetime. PVP acts as a polymer precursor for the formation of an amorphous carbon matrix which wraps the silicon nanoparticles while effectively binding them to the carbon nanotubes. At this point our structure is stable for 200 cycles. While the exact reason that leads to its decay in capacity after 200 cycle has not been identified, our ongoing effort is focused on solving this issue and on achieving stable performance for few thousands cycles. We are exploring the broad parameter space that is available to us (polymer type, silicon nanoparticle size and surface chemistry etc.) to improve the device performance and to identify the mechanisms that negatively affect its stability.

Acknowledgements

This material is based upon work supported by the Winston Chung Global Energy center (http://www.wcgec.ucr.edu/). We also acknowledge partial support from the 3M Company via the Non-tenured Faculty Award. Electron microscope characterization is performed at the Central Facility for Advanced Microscopy and Microanalysis (CFAMM) at UC Riverside.

Appendix A. Supplementary data

Supplementary data related to this article can be found at http://dx.doi.org/10.1016/j.jpowsour.2014.09.155.

References

[1] M.N. Obrovac, L. Christensen, Electrochem. Solid State Lett. 7 (2004) A93–A96.
[2] J.P. Maranchi, A.F. Hepp, P.N. Kumta, Electrochem. Solid State Lett. 6 (2003) A198–A201.
[3] H. Wu, G. Chan, J.W. Choi, I. Ryu, Y. Yao, M.T. McDowell, S.W. Lee, A. Jackson, Y. Yang, L.B. Hu, Y. Cui, Nat. Nanotechnol. 7 (2012) 309–314.
[4] J.C. Guo, A. Sun, X.L. Chen, C.S. Wang, A. Manivannan, Electrochim. Acta 56 (2011) 3981–3987.
[5] C.K. Chan, R. Ruffo, S.S. Hong, Y. Cui, J. Power Sources 189 (2009) 1132–1140.
[6] M. Nie, D.P. Abraham, Y. Chen, A. Bose, B.L. Lucht, J. Phys. Chem. C 117 (2013) 13403–13412.

[7] C. Martin, O. Crosnier, R. Retoux, D. Belanger, D.M. Schleich, T. Brousse, Adv. Funct. Mater. 21 (2011) 3524–3530.
[8] J.H. Ryu, J.W. Kim, Y.E. Sung, S.M. Oh, Electrochem. Solid State Lett. 7 (2004) A306–A309.
[9] C.K. Chan, H.L. Peng, G. Liu, K. McIlwrath, X.F. Zhang, R.A. Huggins, Y. Cui, Nat. Nanotechnol. 3 (2008) 31–35.
[10] C.K. Chan, R.N. Patel, M.J. O'Connell, B.A. Korgel, Y. Cui, ACS Nano 4 (2010) 1443–1450.
[11] L.F. Cui, R. Ruffo, C.K. Chan, H. Peng, Y. Cui, Nano Lett. 9 (2009) 491–495.
[12] T.D. Bogart, D. Oka, X.T. Lu, M. Gu, C.M. Wang, B.A. Korgel, ACS Nano 8 (2014) 915–922.
[13] M.H. Park, M.G. Kim, J. Joo, K. Kim, J. Kim, S. Ahn, Y. Cui, J. Cho, Nano Lett. 9 (2009) 3844–3847.
[14] C. Erk, T. Brezesinski, H. Sommer, R. Schneider, J. Janek, Acs Appl. Mater. Interfaces 5 (2013) 7299–7307.
[15] X.H. Liu, L. Zhong, S. Huang, S.X. Mao, T. Zhu, J.Y. Huang, ACS Nano 6 (2012) 1522–1531.
[16] N. Dimov, S. Kugino, M. Yoshio, J. Power Sources 136 (2004) 108–114.
[17] M.H. Kong, J.H. Noh, D.J. Byun, J.K. Lee, J. Electroceram. 23 (2009) 376–381.
[18] V.G. Khomenko, V.Z. Barsukov, J.E. Doninger, I.V. Barsukov, J. Power Sources 165 (2007) 598–608.
[19] M. Alias, O. Crosnier, I. Sandu, G. Jestin, A. Papadimopoulos, F. Le Cras, D.M. Schleich, T. Brousse, J. Power Sources 174 (2007) 900–904.
[20] C. Martin, M. Alias, F. Christien, O. Crosnier, D. Belanger, T. Brousse, Adv. Mater. 21 (2009) 1–7.
[21] J.K. Lee, K.B. Smith, C.M. Hayner, H.H. Kung, Chem. Commun. 46 (2010) 2025–2027.
[22] K. Evanoff, A. Magasinski, J.B. Yang, G. Yushin, Adv. Energy Mater. 1 (2011) 495–498.
[23] X. Zhou, Y.-X. Yin, L.-J. Wan, Y.-G. Guo, Chem. Commun. 48 (2012).
[24] Y.H. Zhu, W. Liu, X.Y. Zhang, J.C. He, J.T. Chen, Y.P. Wang, T.B. Cao, Langmuir 29 (2013) 744–749.
[25] L. Luo, J. Wu, J. Luo, J. Huang, V.P. Dravid, Sci. Rep. 4 (2014).
[26] W. Wang, P.N. Kumta, ACS Nano 4 (2010) 2233–2241.
[27] S.L. Chou, Y. Zhao, J.Z. Wang, Z.X. Chen, H.K. Liu, S.X. Dou, J. Phys. Chem. C 114 (2010) 15862–15867.
[28] L.F. Cui, L.B. Hu, J.W. Choi, Y. Cui, ACS Nano 4 (2010) 3671–3678.
[29] K. Evanoff, J. Khan, A.A. Balandin, A. Magasinski, W.J. Ready, T.F. Fuller, G. Yushin, Adv. Mater. 24 (2012), 533-+.
[30] L. Mangolini, E. Thimsen, U. Kortshagen, Nano Lett. 5 (2005) 655–659.
[31] O. Yasar-Inceoglu, T. Lopez, E. Farshihagro, L. Mangolini, Nanotechnology 23 (2012) 255604.
[32] R.J. Anthony, D.J. Rowe, M. Stein, J. Yang, U. Kortshagen, Adv. Funct. Mater. 21 (2011) 4042–4046.
[33] L. Mangolini, D. Jurbergs, E. Rogojina, U. Kortshagen, Phys. Status Solidi C 3 (2006) 3975–3978.
[34] X. Li, Y. He, M.T. Swihart, Langmuir 20 (2004) 4720–4727.
[35] W. Chen, Z.L. Fan, A. Dhanabalan, C.H. Chen, C.L. Wang, J. Electrochem. Soc. 158 (2011) A1055–A1059.
[36] J. Graetz, C.C. Ahn, R. Yazami, B. Fultz, Electrochem. Solid State Lett. 6 (2003) A194–A197.
[37] A. Magasinski, P. Dixon, B. Hertzberg, A. Kvit, J. Ayala, G. Yushin, Nat. Mater. 9 (2010) 353–358.
[38] X. Feng, J. Yang, P. Gao, J. Wang, Y. Nuli, RSC Adv. 2 (2012) 5701–5706.
[39] A. Esmanski, G.A. Ozin, Adv. Funct. Mater. 19 (2009) 1999–2010.
[40] M.N. Obrovac, L.J. Krause, J. Electrochem. Soc. 154 (2007) A103–A108.
[41] Y.K. Du, P. Yang, Z.G. Mou, N.P. Hua, L. Jiang, J. Appl. Polym. Sci. 99 (2006) 23–26.
[42] M.F. Silva, C.A. da Silva, F.C. Fogo, E.A.G. Pineda, A.A.W. Hechenleitner, J. Therm. Anal. Calorim. 79 (2005) 367–370.
[43] M.J. O'Connell, P. Boul, L.M. Ericson, C. Huffman, Y.H. Wang, E. Haroz, C. Kuper, J. Tour, K.D. Ausman, R.E. Smalley, Chem. Phys. Lett. 342 (2001) 265–271.
[44] J.B. Gao, A.P. Yu, M.E. Itkis, E. Bekyarova, B. Zhao, S. Niyogi, R.C. Haddon, J. Am. Chem. Soc. 126 (2004) 16698–16699.
[45] H. Richter, Z.P. Wang, L. Ley, Solid State Commun. 39 (1981) 625–629.
[46] V. Paillard, P. Puech, M.A. Laguna, R. Carles, B. Kohn, F. Huisken, J. Appl. Phys. 86 (1999) 1921–1924.
[47] Z. Iqbal, S. Veprek, J. Phys. C Solid State Phys. 15 (1982) 377–392.
[48] C.M. Hessel, J. Wei, D. Reid, H. Fujii, M.C. Downer, B.A. Korgel, J. Phys. Chem. Lett. 3 (2012) 1089–1093.
[49] A.C. Ferrari, J. Robertson, Phys. Rev. B 61 (2000) 14095–14107.
[50] A.C. Ferrari, J. Robertson, Phys. Rev. B 64 (2001).
[51] A.C. Ferrari, J. Robertson, Philos. Trans. R. Soc. A 362 (2004) 2477–2512.
[52] W.S. Bacsa, J.S. Lannin, D.L. Pappas, J.J. Cuomo, Phys. Rev. B 47 (1993) 10931–10934.
[53] F. Li, J.S. Lannin, Appl. Phys. Lett. 61 (1992) 2116–2118.
[54] C.S. Casari, A.L. Bassi, A. Baserga, L. Ravagnan, P. Piseri, C. Lenardi, M. Tommasini, A. Milani, D. Fazzi, C.E. Bottani, P. Milani, Phys. Rev. B 77 (2008).
[55] A.C. Ferrari, J. Robertson, Phys. Rev. B 63 (2001).
[56] Z. Hu, X. Liao, H. Diao, G. Kong, X. Zeng, Y. Xu, J. Cryst. Growth 264 (2004) 7–12.
[57] T. Rajagopalan, X. Wang, B. Lahlouh, C. Ramkumar, P. Dutta, J. Appl. Phys. 94 (2003) 5252–5260.
[58] D. Song, E.C. Cho, Y.H. Cho, G. Conibeer, Y. Huang, S. Huang, M.A. Green, Thin Solid Films 516 (2008) 3824–3830.
[59] D.Y. Song, E.C. Cho, G. Conibeer, C. Flynn, Y.D. Huang, M.A. Green, Sol. Energy Mater. Sol. Cells 92 (2008) 474–481.
[60] M.H. Brodsky, M. Cardona, J. Non-Cryst. Solids 31 (1978) 81–108.
[61] U. Kasavajjula, C.S. Wang, A.J. Appleby, J. Power Sources 163 (2007) 1003–1039.
[62] I.S. Kim, G.E. Blomgren, P.N. Kumta, J. Power Sources 130 (2004) 275–280.